Role of low-order proper orthogonal decomposition modes and large-scale coherent structures on sediment particle entrainment

Johannes Schobesberger, Dominik Worf, Petr Lichtneger, Sencer Yücesan, Christoph Hauer, Helmut Habersack & Christine Sindelar

Published online: 06 Apr 2021.

Submit your article to this journal ☑

Article views: 266

View related articles ☑

View Crossmark data ☑

Research paper

Role of low-order proper orthogonal decomposition modes and large-scale coherent structures on sediment particle entrainment

JOHANNES SCHOBESBERGER (IAHR Member), PhD Student, *Christian Doppler Laboratory for Sediment Research and Management, Institute of Hydraulic Engineering and River Research, University of Natural Resources and Life Sciences, Vienna, Austria*
Email: johannes.schobesberger@boku.ac.at (author for correspondence)

DOMINIK WORF , PhD Student, *Institute of Hydraulic Engineering and River Research, University of Natural Resources and Life Sciences, Vienna, Austria*
Email: dominik.worf@boku.ac.at

PETR LICHTNEGER, Senior Scientist, *Christian Doppler Laboratory for Sediment Research and Management, Institute of Hydraulic Engineering and River Research, University of Natural Resources and Life Sciences, Vienna, Austria*
Email: petr.lichtneger@boku.ac.at

SENCER YÜCESAN (IAHR Member), PhD Student, *Christian Doppler Laboratory for Sediment Research and Management, Institute of Hydraulic Engineering and River Research, University of Natural Resources and Life Sciences, Vienna, Austria*
Email: s.yuecesan@boku.ac.at

CHRISTOPH HAUER (IAHR Member), Senior Scientist, *Christian Doppler Laboratory for Sediment Research and Management, Institute of Hydraulic Engineering and River Research, University of Natural Resources and Life Sciences, Vienna, Austria*
Email: christoph.hauer@boku.ac.at

HELMUT HABERSACK (IAHR Member), Professor, *Institute of Hydraulic Engineering and River Research, University of Natural Resources and Life Sciences, Vienna, Austria*
Email: helmut.habersack@boku.ac.at

CHRISTINE SINDELAR (IAHR Member), Senior Scientist, *Institute of Hydraulic Engineering and River Research, University of Natural Resources and Life Sciences, Vienna, Austria*
Email: christine.sindelar@boku.ac.at

ABSTRACT
This study presents experimental investigations of entrainment events of a single sediment particle resting in a small pocket on a smooth bed in an open channel flow. The data were acquired with a tomographic particle tracking velocimetry system. The shake the box algorithm, a spatially high resolved Lagrangian tracking method, was applied to determine time-resolved and three-dimensional flow velocities in a volume during particle entrainment. The proper orthogonal decomposition (POD) method was applied to identify motions in the flow field carrying the most turbulent kinetic energy (TKE). Based on the POD method, the most energetic flow structures were linked with the occurring quadrant events at particle entrainment. It was shown that particle entrainment follows TKE peaks based on low-order POD modes caused by large sweeps. Two streamwise elongated counter rotating vortices with emerging sweeps in between were observed during particle entrainment. Here, most of the TKE exists in the first POD mode. This signature is suggested to be part of very large-scale coherent motions.

Keywords: Coherent structures; fluid–particle interactions; proper orthogonal decomposition; sediment entrainment; shake the box; tomographic particle tracking velocimetry; turbulent kinetic energy

1   Introduction

Semi-empirical equations for describing sediment entrainment and sediment transport (Meyer-Peter & Mueller, 1948; Shields, 1936; Smart & Jaeggi, 1983) are mostly based on averaged flow parameters, especially on the shear stress. If the shear stress exceeds a certain threshold value, which is often referred to as the critical shear stress, sediment movement is assumed. However, instantaneous flow structures that lead to peak events regarding the streamwise velocity, drag force and lift force, rather than the average flow conditions (e.g. time averaged shear stress), result in sediment entrainment under the threshold conditions of motion (Diplas et al., 2008; Valyrakis et al., 2010). Experimental and numerical investigations (Celik et al., 2013; Diplas & Dancey, 2013; Dwivedi et al., 2011; Schobesberger et al., 2020; Vowinckel et al., 2016; Wu & Shih, 2012) have shown that the entrainment of single particles is mostly caused by coherent motions, which are often associated with so-called hairpin vortices. While coherent structures in the form of hairpin vortices and the autogeneration mechanism are well observed in the near-wall region (Kline et al., 1967), the formation of and the interaction between large- and very large-scale coherent structures are not fully understood. Researchers (Adrian et al., 2000; Bagherimiyab & Lemmin, 2018; Deng et al., 2018; Hurther et al., 2007; Wu & Christensen, 2010; Zhong et al., 2015) have reported the existence of large-scale coherent motions (LSMs), large-scale coherent shear stress structures (LC3Ss) and very large-scale motions (VLSMs) in their studies. LSMs can extend up to the free water surface and reach a size of up to 2–3 times the water depth in the streamwise direction (Adrian, 2007; Adrian & Marusic, 2012). Structures with a larger extent are further referred to as VLSMs. While the physics behind these structures has been the focus of research, little is known about the influence of these motions (especially LSM and VLSM) on sediment particle entrainment and sediment transport as well as the evolution of bed forms.

Based on tomographic particle tracking velocimetry (TOMO-PTV) measurements, Schobesberger et al. (2020) reported the presence of large-scale coherent structures in the form of symmetric and asymmetric hairpin vortices during single sediment particle entrainment. These coherent motions had a vertical extent up to 60% of the water depth and consisted of a group of hairpin structures. Diplas et al. (2008) introduced the impulse concept for describing the particle entrainment process, considering not only the peak of the acting forces on a particle but also the duration of the peak event. Yücesan et al. (2020) used the same flow conditions and geometry of the sediment particle as in the experiments of Schobesberger et al. (2020) in their large eddy simulation (LES). Yücesan et al. (2020) conducted a quadrant analysis initially proposed by Lu and Willmarth (1973) for a statistical description of coherent structures during the highest observed impulses on the sediment particle. The quadrants represented outward interaction QI ($u' > 0$ and $v' > 0$), ejections QII ($u' < 0$ and $v' > 0$), inward interactions QIII ($u' < 0$ and

$v' < 0$) and sweeps QIV ($u' > 0$ and $v' < 0$). During the highest impulses, mostly QI and QIV were observed. Here, u' and v' correspond to streamwise and vertical velocity fluctuations. Furthermore, Yücesan et al. (2020) studied the influence of coherent motions on the drag coefficient. While small-scale structures within the viscous layer resulted in negligible changes, large-scale structures in the outer layer increased the drag coefficient up to 19%. This result fits the observations of the Schobesberger et al. (2020) experiment, where large-scale coherent structures were found to be the decisive structures during sediment particle entrainment.

Nevertheless, there is difficulty in differentiating which coherent structures influence sediment particle entrainment and which parameters are suitable for their description. For example, Cameron et al. (2017) observed a bimodal distribution in the pre-multiplied spectrum of streamwise velocity fluctuations in open channel flows, revealing the presence of LSMs and VLSMs. Furthermore, Cameron et al. (2019) estimated the influence of VLSMs on the drag forces and pressures placed on fixed spherical roughness elements. The Cameron et al. (2019) results indicate that sediment particle entrainment may relate to the passage of low-pressure events during high-velocity flow regions related to VLSMs. The experiments and the methods used by Cameron et al. (2019) provide important statistical information about VLSMs and on the relationship to relevant parameters (such as the drag force) for describing sediment particle entrainment. To go one step further, it becomes necessary to conduct experiments with mobile sediment particles and use approaches that can verify the influence of coherent structures (e.g. LSM and VLSM) during sediment particle entrainment.

However, identifying coherent structures in experimental data (e.g. from particle image velocimetry – PIV) or numerical data (e.g. from LES, DNS) is not an easy task, as they are often hidden behind incoherent structures (Kostas et al., 2005). To separate these structures, proper orthogonal decomposition (POD) could be a well-suited method. While POD is common in the field of fluid mechanics, this method is rarely applied in the field of sediment research.

POD was introduced as a mathematical tool for the decomposition of data into spatiotemporal modes (Holmes et al., 1996). Berkooz et al. (1993), Lumley (1967) and Holmes et al. (1996) used this method, also known as the Karhunen–Loeve decomposition, for studying turbulent flows, as this method identifies motions in the flow field containing the most energy on average. One of the advantages of the POD method is that it can be used as a kind of filter to distinguish between highly turbulent kinetic energy (TKE) zones and less TKE zones in the flow field. While lower-order spatial POD modes correspond to high energetic flow features and larger scaled motions (e.g. VLSM), high-order spatial POD modes are related to fewer energy-containing flow features and smaller scaled motions in the flow field (Holmes et al., 1996). Under the assumption that POD modes with a certain amount of energy contribute to coherent structures, Lumley
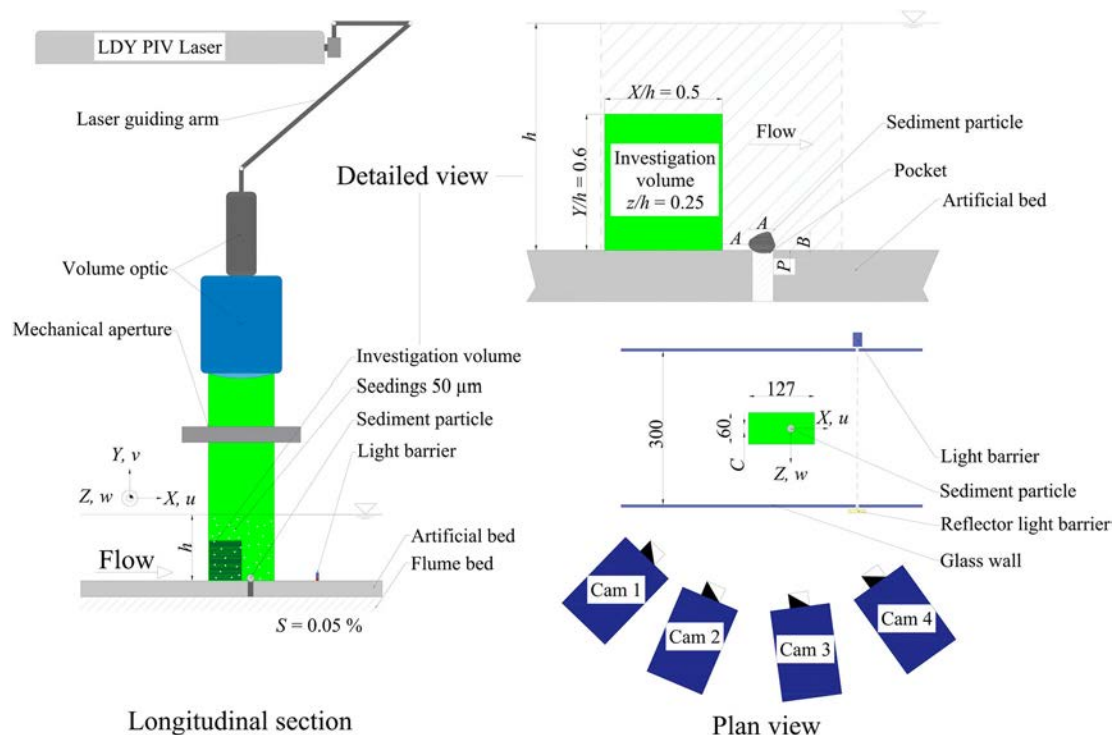
Figure 1　Experimental set-up and measurement system. Dimensions are in millimetre (mm)

(1967) first used this method in an investigation. Because of the high computational effort of the classic POD method, Sirovich (1987) introduced the snapshot method (Section 3.2).

POD delivers time-resolved data corresponding to temporal modes and spatial modes. For normalized spatial modes, the squares of the temporal modes provide information about the amount of TKE of each spatial mode at each time step. Therefore, it is possible to investigate dominant flow structures at the moment of sediment particle entrainment (in the time domain), in contrast to other approaches such as the power spectral density. Here, the time relation is lost due to frequency domain transformation by using long term measurements.

In this study, the influence of large- and very large-scale motions occurring during sediment particle entrainment, filtered based on the POD method, is investigated experimentally. In contrast to other experimental studies, where mainly single-point or 2D measurements in a plane (laser Doppler velocimetry LDV or 2D PIV) were conducted, this study is based on time-resolved volumetric data. The data for the analysis were obtained from tomographic particle tracking velocimetry. The shake the box algorithm, a spatially highly resolved Lagrangian tracking method, was used to calculate time-resolved and three-dimensional velocities in a volume. To further analyse the data during sediment particle entrainment, three methods were applied: (i) decomposition of the velocity data into POD modes; (ii) quadrant analysis to link the dominant TKE events obtained from POD with coherent structures; and (iii) visualization of the dominant three-dimensional coherent structures with iso-surfaces based on the Q_c.

2 Experimental and measurement set-up

The experiments were conducted in the hydraulic lab at the University of Natural Resources and Life Sciences in Vienna. A tilting hydraulic flume with a length of 12.5 m and a width of 0.3 m was used. For all the experiments, the slope S was set to 0.05%. The sidewalls of the flume are made of glass. The flume has an internal water cycle that is equipped with a speed-controlled pump. The discharge was measured by an electromagnetic flow sensor (IDM) with an accuracy of 0.1%. Laminated wooden panels were used as a bed in the flume. Compared to gravel beds or idealized spherical beds the used wooden panels can be described as a smooth bed. The hydraulic conditions for the experiments are in the transitionally rough regime. The smooth bed was chosen to avoid sediment particle entrainment initiated by random turbulence peaks or flow separations behind roughness elements as it can be the case over rough beds. Schmeeckle et al. (2007) concluded that especially the drag coefficients of spheres used as particle and roughness elements are not suitable for sediment transport models. Therefore, the used particle was chosen to be a fluvial sediment particle from the Danube River with dimensions of $A = 13$ mm (in streamwise direction), $B = 11$ mm (bed normal or vertical direction) and $C = 14$ mm (spanwise direction). The pocket for the sediment particle was located seven metres downstream of the flume inlet and in the flume axis. The pocket was made from concrete and had the shape of the sediment particle's imprint at a depth of $P = 2$ mm. This ensured the same positioning of the particle for all experiments. Figure 1 shows the experimental set-up.

2.1   *Implementation of TOMO-PTV and the shake the box algorithm*

The TOMO-PTV system was used to acquire the u/v/w velocities in the X/Y/Z direction, where u is the streamwise (X) velocity component, v is the vertical (Y) velocity component and w is the spanwise (Z) velocity component. Particle images were acquired first, and then particle tracks were calculated using specific processing procedures; based on the tracks, the velocity components could be approximated on the chosen Cartesian grid. The TOMO-PTV arrangement consisted of a high-speed double-pulsed laser, four high-speed cameras in a linear configuration, a timing box (PTU X — for synchronizing the laser pulses with the image recording) and a PC, all from LaVision GmbH (Goettingen, Germany). Polyamide particles with a mean diameter of 50 μm and a density of 1.016 g cm^{-3} were applied as the seeding. The laser beam was expanded with volume optics to a size of X/Y/Z = 127/120/60 mm entering the measurement region from the top. A mechanical aperture was used for sharpening the edges of the laser volume. Thanks to a relatively smooth water surface (without waves influencing the quality of laser lightening), no additional phase interface (e.g. a submerged glass box as in Lichtneger et al., 2020) was necessary. A single-frame recording mode was applied with a frame rate of 800 Hz to achieve sufficiently time-resolved data. Because of the internal storage capacity limitations of the high-speed cameras (18 GB/cam), the maximum number of frames was 6123, and the maximum acquisition time was approximately 7.65 s. A detailed summary of the main technical and measurement parameters used is presented in Table 1. The laser volume covered 80 mm upstream and 47 mm downstream of the particle centres. Concerning the spanwise alignment, the particle was sighted in the centre of the laser volume. A light barrier was mounted 200 mm downstream of the particle (outside the field of view of all cameras) to trigger the onset of particle movement. This was done with an A/D electronic device (ADC-250-PCle) for external signals which was integrated in the timing unit. If the sediment particle was entrained and crossed the light barrier, a signal post-triggered the TOMO-PTV measurement system, where a ring buffer was running. Based on these adjustments, particle entrainment occurred around frame 5300 or after 6.6 s. A sliding minimum of 7 pixels was subtracted, and the stored images were normalized with a local average of 300 pixels. Furthermore, Gaussian smoothing over 3 × 3 pixels and sharpening were applied.

The calibration was carried out with a 3D-calibration plate (La Vision Type 204-15) consisting of two planes with calibration markers. The transverse distance between the planes of the calibration target was 3 mm. A third-order polynomial fit model was applied. The calibration error resulted in 0.26, 0.27, 0.22 and 0.27 pixels for cameras one to four, respectively. Furthermore, the so-called volume self-calibration, introduced by Wieneke (2008), was conducted, leading to reduced calibration errors of 0.01 pixels for each camera. This

Table 1   Laser equipment and additional measurement characteristics

Parameter	Quantity
Laser	• LDY PIV laser (Double Cavity High Speed Laser, Litron)
	• 30 mJ output energy
	• 527 nm wavelength
	• 1000 Hz repetition rate
Four high-speed cameras	• Imager Pro HS 4M CMOS
	• Maximum repetition rate of 1300 Hz at max. resolution
	• Maximum resolution of 2016 × 2016 pixels
	• 12-bit digital output
	• Pixel size 11 μm
Timing Box	• PTU X High Speed
A/D electronic for external signals	• Type ADC-250-PCle
Calibration target	• La Vision Type 204-15
Lenses (#f)	• 16
Objectives	• 85 mm focal length (Zeiss)
Image Rate	• 0.8 kHz
Number of frames per camera	• 6123
Image Size	• 1488 × 1400 pixels
Size of laser volume X/Y/Z	• 127/120/60 mm
Flow seeding particles	• Polyamide particles
	• Diameter of 50 μm
	• Density of 1.016 g cm^{-3}
Seeding density	• 0.04 ppp (particles per pixel)
Particle shift	• Maximum 10 voxels (three-dimensional pixel)
Light barrier	• Reflection light barrier Sick WL8

is well below the proposed value of 0.1 pixels (Wieneke, 2008).

The "shake the box" (STB) algorithm was used to determine the velocities. STB is based on Lagrangian particle tracking and was introduced by Schanz et al. (2013). Based on the STB algorithm, it is possible to use seeding densities up to 0.1 ppp (particles per pixel), which is approximately 20 times higher than for conventional 3D-particle tracking velocimetry (3D-PTV with 0.005 ppp) and similar to tomographic particle image velocimetry TOMO-PIV. The computational time is approximately five to 50 times lower compared to TOMO-PIV.

For calculating the STB, the threshold for particle detection was set to 30 light intensity counts. To give a reference value, the average intensity in the measurement volume after image post-processing was approximately 15 counts. The allowed triangulation error was set to 1.8 voxels, and the maximum particle shift was set to 10 voxels. The shake delta was set to 0.2 voxels, which represents the "shake" distance around the predicted particle position. With these adjustments, a total number of approximately 24,000 particle tracks per time step was achieved. Subsequently, the trajectories were fitted to a

regular grid with (i) a subvolume size of 64 voxels; (ii) an overlap of 75%; and (iii) a minimum number of three particles resulting in a regular grid of a $16 \times 16 \times 16$ voxel or $1.5 \times 1.5 \times 1.5$ mm. The track conversion was calculated with a second-order polynomial fit at a minimum filter length of three time steps.

To calculate the uncertainty of the fitted particle tracks to a regular grid, the "track benchmarking method" introduced by Schneiders and Sciacchitano (2017) was used. Applying this method to the recorded data in this paper, the relative uncertainty of all measurements ranged between 0.187% and 0.19%, 0.186% and 0.191%, and 0.332% and 0.385% for the streamwise velocity u, the vertical velocity v and the spanwise velocity w, respectively.

2.2　*Threshold conditions of particle entrainment*

To determine the threshold conditions of sediment particle entrainment, a total of 52 experiments were carried out. First, 44 mobilization tests were exclusively used to determine the flow conditions during entrainment. Therefore, the sediment particle was placed in the pocket at a constant discharge Q of $19.6 \, \mathrm{l \, s^{-1}}$. Then, the water level, which was controlled with a tail gate at the end of the flume, was lowered gradually in steps of 1–2 mm. It took approximately 30 s to obtain a steady water level after each lowering step. The water level was then kept constant for 10 min. After a successful particle entrainment experiment the water level was increased for decreasing the flow velocity. This made it possible to replace the sediment particle into the pocket for the next mobilization test. If the sediment particle did not move within 10 min, the water level was lowered further until entrainment occurred. The water levels were measured with a manual gauge at two points in the flume axis, 2.8 m upstream and 0.8 m downstream of the sediment particle. The differences in water depths h at the two positions resulted in a deviation of less than 0.2 mm. The resulting changes in the mean flow velocity lie within the uncertainty of the PTV measurement system. The entrainment conditions of the mobilization tests (#44) are shown in Fig. 2. It can be seen (Fig. 2) that sediment particle entrainment occurred in a certain range concerning the water depth h. Overall, the fluctuations of the water depth h during entrainment, expressed as standard deviation, were ± 2.8 mm at the same discharge Q, slope S and sediment particle positions. Based on observations of the preliminary experiments, the sediment particle movement was characterized as rolling.

A total of eight TOMO-PTV tests (named 1S to 8S) were carried out, under the same flow conditions regarding discharge Q, slope S and sediment particle position (marked by crosses in Fig. 2). The water level h was adjusted to the mean water level $\bar{h}$ resulting from the mobilization tests (compare to Fig. 2). In the TOMO-PTV experiments, the time until sediment particle entrainment was also recorded. In addition to the tests with sediment particle entrainment, another test was conducted without a sediment particle but under the same hydraulic conditions. This
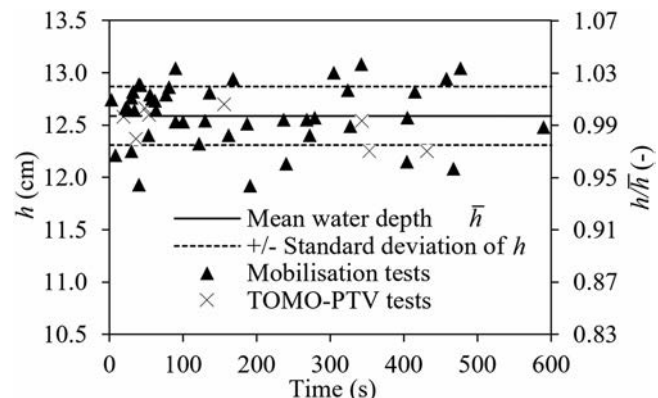

Figure 2　Summarized sediment particle entrainment tests. Triangles correspond to the mobilization tests, while the crosses correspond to the TOMO-PTV tests. Here h (cm) is the water depth and $\bar{h}$ (cm) the mean water depth of all conducted tests

test is referred to as the reference case (RF) and allows a comparison between the flow with and without sediment particles (entrainment).

Based on the tests, the following parameters were calculated: (i) Reynolds number $\mathsf{R_e} = 65{,}000$ ($\mathsf{R_e} = Uh/v$); (ii) Froude number $\mathsf{F} = 0.48$ ($\mathsf{F} = U/\sqrt{gh}$); (iii) particle Reynolds number ($\mathsf{R_{e^*}} = u^*d/v$); and (iv) Shields parameter θ ($\theta = \tau/(\rho_s - \rho)gd$). Here, U describes the mean flow velocity, g is the gravity, v is the kinematic viscosity, u^* is the shear velocity ($u^* = \sqrt{\tau/\rho}$) and τ is the bed shear stress ($\tau = \rho g R S$). Here, ρ_w describes the water density and R describes the hydraulic radius. The water temperature was measured during the experiments, resulting in $v = 1.01 \times 10^{-6}$ and density $\rho = 998.21 \, \mathrm{kg \, m^{-3}}$. The density of the sediment particle ρ_s was assumed to be $2650 \, \mathrm{kg \, m^{-3}}$. Table 2 shows the flow conditions of the RF and the tests with sediment particle entrainment (S), measured with TOMO-PTV, at the highest and lowest water depths marked with the "upper" and "lower" limits in Table 2.

Based on the calculated particle Reynolds number $\mathsf{R_{e^*}} \sim 218$ (Table 2), the critical Shields parameter was approximately $\theta_c = 0.03$ according to the Shields diagram (Shields, 1936). The calculated Shields parameters θ were approximately 10 times lower (Table 2). In this paper, a smooth flume bed was used, and the sediment particle was exposed to the flow. The applicability of the Shields criterion might be questioned, but it is given here for comparison with other studies.

3　Turbulence statistics and implementation of POD

As shown in Fig. 1, the "investigation volume" for calculating the POD had a length in the streamwise direction (X) of 70 mm and a width in the spanwise direction (Z) of 30 mm. The upstream distance between the particle and the downstream end of the investigation volume for the POD calculation is equal to the length of the particle in the streamwise direction. This distance was chosen to avoid any influence, such as deceleration, upstream of the particle in the "investigation volume" and was

Table 2   Summary of the flow conditions, where Q is the discharge (l s^{-1}), h is the water depth (cm), U is the mean streamwise velocity (m s^{-1}), τ is the shear stress (N m^{-2}), u^* is the shear velocity (m s^{-1}), θ is the dimensionless Shields parameter and R_{e*} is the particle Reynolds number

	Q (l s^{-1})	h (cm)	U (m s^{-1})	τ (N m^{-2})	u^* (m s^{-1})	θ (–)	R_{e*} (–)
RF	19.6	12.6	0.52	0.336	0.0183	0.0031	217.6
S lower limit	19.6	12.3	0.53	0.331	0.0182	0.0030	216.1
S upper limit	19.6	12.7	0.51	0.337	0.0184	0.0031	218.0

also used by e.g. Dwivedi et al. (2010, 2011) and Schmeeckle et al. (2007). Based on the investigations of Schobesberger et al. (2020), coherent structures, during particle entrainment, had a vertical extension of approximately $Y/h = 0.6$. This vertical extension was also used for tests in this paper.

3.1   *Turbulence statistics*

To compare the flow with existing literature, e.g. Nezu and Nakagawa (1993), double averaged time and spatial turbulence intensities σ of the streamwise $\langle \sigma_u \rangle$, vertical $\langle \sigma_v \rangle$ and spanwise $\langle \sigma_w \rangle$ velocities components were calculated. Time averaging was performed over the whole measurement period, while spatial averaging was calculated in the streamwise X direction and spanwise Z direction in the investigation volume. The turbulence intensities $\langle \sigma_{u,v,w} \rangle$ were normalized with the shear velocity u^* (Fig. 3).

Figure 3 shows the experimental normalized turbulence intensities $\langle \sigma_u \rangle / u^*$, $\langle \sigma_v \rangle / u^*$ and $\langle \sigma_w \rangle / u^*$ compared to the empirical investigations of Nezu (1977), which are well accepted in the field of open channel flows. The dashed lines in Fig. 3 represent the semi-theoretical curves from Nezu (1977). While the normalized turbulence intensities in the streamwise and spanwise directions are in the range of the determined values of Nezu (1977), the vertical turbulence intensities in the range of $Y/h = 0$ to 0.2 are lower. A reason for the lower values concerning the vertical turbulence intensities closer to the bed might be that in this region, the growth of eddies is influenced by the flume bed. Similar observations were made by Bagherimiyab
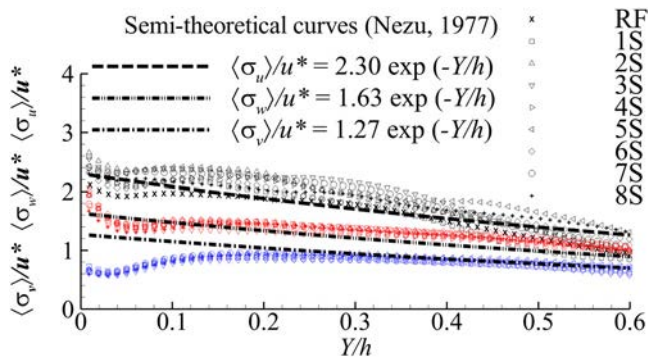

Figure 3   Turbulence intensities normalized with the shear velocity u^* of all tests (RF and 1S to 8S) measured with TOMO-PTV. Grey, red and blue symbols correspond to $\langle \sigma_u \rangle / u^*$, $\langle \sigma_w \rangle / u^*$ and $\langle \sigma_v \rangle / u^*$, respectively. The symbols describe the conducted tests RF, 1S to 8S and are explained in the legend. The dashed lines correspond to the semi-theoretical curves of Nezu (1977)

and Lemmin (2018) and Dwivedi et al. (2011). The cumulative moving average was calculated to verify the velocity averages. At two chosen points located in the measurement volume, streamwise velocities were extracted from the reference test data. The two points were in the middle of the measuring volume regarding the streamwise and spanwise directions at heights of $Y/h = 0.2$ and $Y/h = 0.6$, respectively. For both points, the fluctuations in the streamwise average values were less than 0.7% after a time period of 3.75 s. Hence, steady flow conditions with a time scale < 3.75 s could be assumed during the tests and at the time of sediment particle entrainment.

3.2   *Implementation of proper orthogonal decomposition (POD)*

To calculate the POD, all three velocity components in the investigation volume were considered in this paper. First, time averaged velocities U, V and W were subtracted from the instantaneous velocities u, v and w to achieve instantaneous fluctuating velocities u', v' and w'.

The POD method decomposes velocity data into the so-called spatial modes ϕ_k and temporal modes a_k. It uses M snapshots u_n of the velocity data on N spatial points. These are combined as columns in a matrix $\mathbf{U}$ leading to $\mathbf{U} \in \mathbb{R}^{3N \times M}$. To obtain the spatial modes, the eigenvalue problem must be solved:

$$\mathbf{R}\,\alpha_k = \mathbf{U}^T \mathbf{U}\alpha_k = \lambda_k \alpha_k, \qquad (1)$$

where the eigenvalues λ_k are arranged in descending order. Due to this ordering, the lowest order modes describe the highest amount of the TKE of the snapshots (Holmes et al., 1996). The computational savings of the snapshot method come into effect here. The matrix $\mathbf{R}$ is in $\mathbb{R}^{M \times M}$, and because M is a much smaller number than $3N$, the eigenvalue problem becomes easier to solve. The spatial modes are defined as:

$$\phi_k := \frac{\mathbf{U}\alpha_k}{||\mathbf{U}\alpha_k||}. \qquad (2)$$

Due to the orthogonality of the eigenvectors α_k the spatial modes form an orthonormal system. The projection $\mathbf{P}u$ of any given vector u onto the subspace spanned by the spatial modes can be described by the linear combination:

$$\mathbf{P}u = \sum_{k=1}^{M} b_k \phi_k = \mathbf{\Phi}b \qquad (3)$$

where the coefficient vector b is, due to the orthogonality of the spatial modes, given by:

$$b = \Phi^T u. \qquad (4)$$

The temporal mode a_k for the spatial mode ϕ_k is defined as the kth row of the coefficient matrix $\mathbf{A}$ of the snapshot matrix $\mathbf{U}$:

$$a_k := (\mathbf{A})_{\mathbf{k}} := (\Phi^{\mathbf{T}}\mathbf{U})_{\mathbf{k}}. \qquad (5)$$

Using the projection onto the subspace spanned by the spatial modes one can approximate the entirety of the velocity data, which leads to a large saving of memory with a minimum of lost information.

When calculating the TKE within an approximated vector of velocity data $\mathbf{P}u$ we obtain:

$$\frac{1}{2}\mathbf{P}u \cdot \mathbf{P}u = \frac{1}{2}\sum_{k,i}^{M} b_k b_i \phi_k \cdot \phi_i = \frac{1}{2}\sum_{k}^{M} b_k b_k, \qquad (6)$$

due to the spatial modes being an orthonormal system. Thus, the TKE in the kth mode of the vector u is $1/2(b_k)^2$ and the TKE in the kth mode for the snapshots is given by half the element-wise square of the kth temporal mode a_k. The equations used in Section 3.2 are based on Holmes et al. (1996) and Sirovich (1987).

A requirement for the application of the snapshot method is that the number of spatial points $3N$ must exceed the number of snapshots M (Saha et al., 2017; Sirovich, 1987). The number of used snapshots was $M = 613$ and the number of spatial points in the investigation volume was $N = 46,483$, and thus the requirement $M < N$ was fulfilled. In this paper snapshots were extracted from all data $M_{all} = 6123$ using an increment of 10. This was done to reduce the computational effort. The changes between M and M_{all} considering the difference in the TKE are less than 0.6% for the lowest 10 spatial modes.

4　Results

The eight TOMO-PTV tests where sediment particle entrainment occurred are labelled as 1S to 8S. RF represents the reference case.

4.1　Cumulative and relative energy of the spatial modes

The cumulative TKE and the relative TKE of the spatial modes were calculated (Eq. 6) over the entire investigation volume for each test, 1S to 8S and RF (Fig. 4a and b). The number of the lowest modes containing at least 50% of the cumulative energy ranges between 5 (for test case 3S) and 12 (for the RF). This is in line with investigations of Saha et al. (2017). As the lower spatial modes contain more energy and are related to large-scale coherent motions (Liu et al., 2001), the mode number (*X*-axis) in Fig. 4a and b was restricted to mode 100. For a better visibility of the data, the *X*-axis is plotted logarithmically. Figure 4a shows the cumulative TKE in per cent, and it is visible that all test cases with sediment particle entrainment 1S to 8S contain more TKE in the lower modes than the reference case, which is marked with the dashed line. After approximately 20 modes, the cumulative energy of the RF exceeds the cumulative energy of test case 1S, which had the least cumulative TKE compared to the other tests with sediment particle entrainment.

Figure 4b shows the relative energy of each mode, and it is visible that the first mode of the test cases with sediment particle entrainment (1S–8S) contains more TKE compared to the RF. The amount of TKE of the first mode varies between 23 and 39% for the test cases with sediment particle entrainment, while the first mode of the RF covers just 17% of the total TKE. Furthermore, it is visible that during the first five modes, the TKE drops rapidly to less than 3.4% for all cases.

4.2　Temporal modes and energy during sediment particle entrainment

Based on the results of Fig. 4b, where the first spatial mode for the tests with sediment particle entrainment covers more energy than the first spatial mode for the RF case, an investigation of the first temporal mode was conducted. The temporal modes for tests 1S-8S were calculated. In Fig. 5, the first temporal mode a_1 is shown, where the vertical dashed line marks the time of sediment particle entrainment (te). For all tests, except for test 6S, a maximum or local peak in the positive coefficient value $a_{1,te}$ is visible at the time of sediment particle entrainment. Test
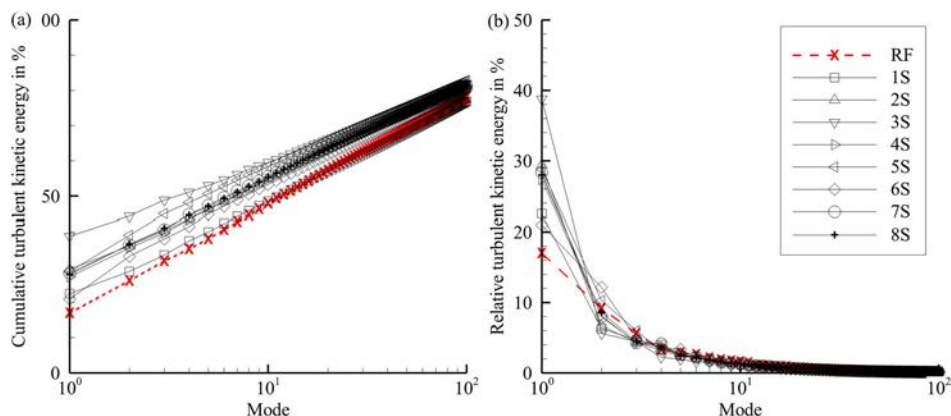

Figure 4　Cumulative TKE (a) and relative TKE (b) of the spatial POD modes for each test and the reference case. The symbols describe the conducted tests RF, 1S to 8S and are explained in the legend. A logarithmic scale is used
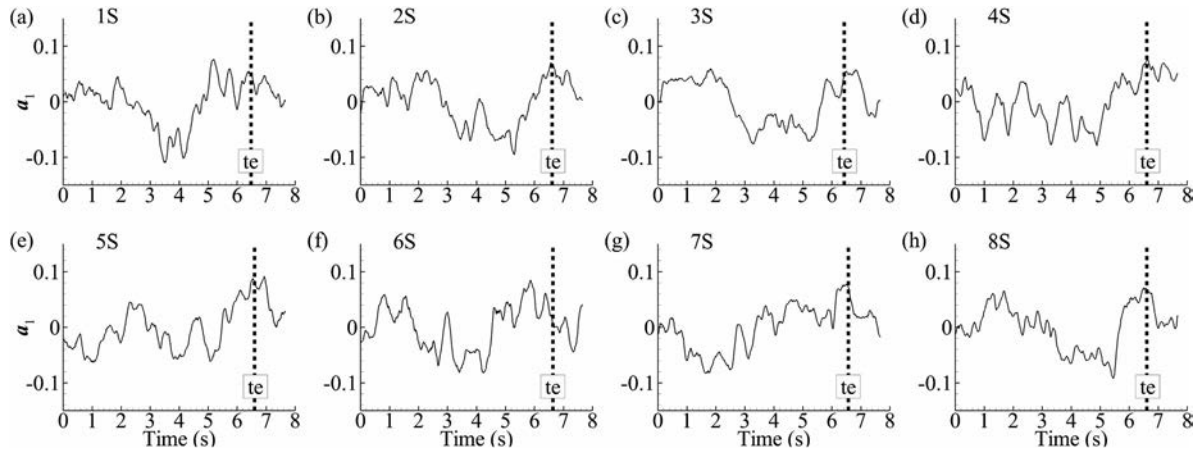
Figure 5   First temporal mode a_1 of the tests with sediment particle entrainment (a) 1S, (b) 2S, (c) 3S, (d) 4S, (e) 5S, (f) 6S, (g) 7S and (h) 8S. The dashed line marks the time of entrainment (te)
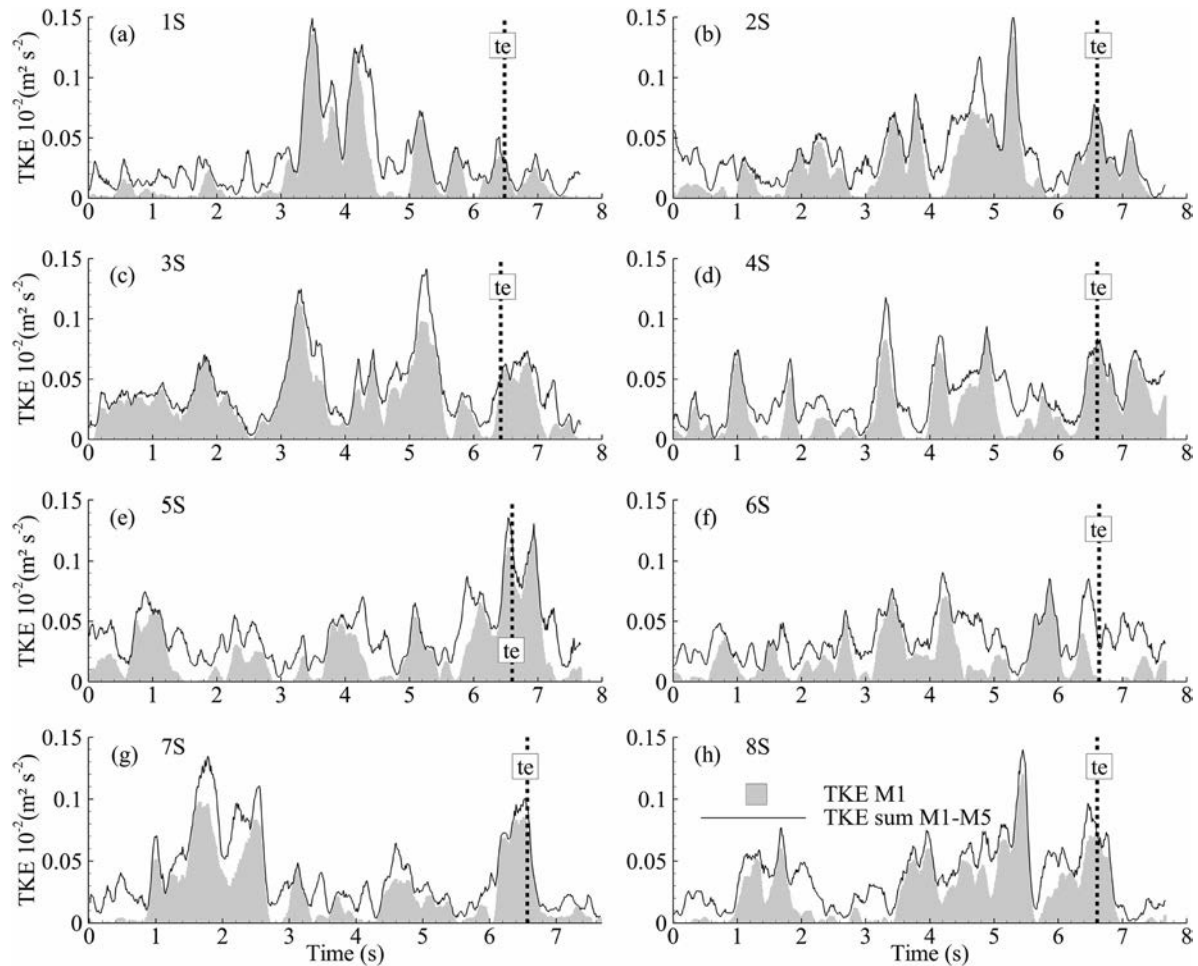

Figure 6   Summed turbulent kinetic energies (TKE) for the first five modes *M* (black lines) of the tests with sediment particle entrainment (a) 1S, (b) 2S, (c) 3S, (d) 4S, (e) 5S, (f) 6S, (g) 7S and (h) 8S. The grey shaded area shows the TKE contribution of only the first temporal mode *M*. The dashed line marks the time of entrainment (te)

6S is an exception. Here, the coefficient value $a_{1,te}$ of the first temporal mode a_1 is close to zero.

The turbulent kinetic energies of the first five temporal modes were calculated based on Eq. (6) to compare the proportions of the temporal modes. Figure 6 shows the turbulent kinetic energies for the first temporal mode (grey shaded area) as well as the

cumulative energy of the first five temporal modes (solid line) for all tests. It is visible that for all tests, except for test 6S, particle entrainment again occurred at a peak value regarding the cumulative TKE (black line in Fig. 6). This is not surprising, as the first spatial mode covers the most energy, and sediment particle entrainment appeared at positive peak coefficient values

of the first temporal mode (Fig. 5). In Fig. 6, it is visible that for these tests, the TKE of the first temporal mode more or less covers the entirety of TKE of the first five temporal modes at the time of sediment particle entrainment. Instead of the high peak events during particle entrainment observed in Fig. 5 for all tests, except for test 6S, the TKE of the first five temporal modes shows peak events but not the maximum TKE containing events at particle entrainment. Only test 5S shows a maximum peak regarding the TKE at the time of sediment particle entrainment. For test case 6S, the TKE hardly contributes to the cumulative energy of the first five modes at sediment particle entrainment. By comparing the peaks of the negative coefficient values of the first temporal modes in Fig. 5 with the peaks of the cumulative turbulent kinetic energies in Fig. 6, it becomes evident that the negative peaks regarding the first temporal modes match with the highest peak events concerning the cumulative turbulent kinetic energies.

To investigate which temporal mode contributes the most to the TKE at sediment particle entrainment, Table 3 compares the contribution of the individual temporal modes to the cumulative TKE of the first five temporal modes. The first temporal mode covers, except for test 6S, more than 79% of the cumulative TKE based on the first five temporal modes. Test 4S shows the highest proportion of mode 1 with 96.20%. An exception concerning the distribution of the TKE is test 6S. Here, the first temporal mode contains only 0.37% of the cumulative TKE, while the second and fourth temporal modes are dominant with 27.03 and 65.78%, respectively.

4.3   *Quadrants during sediment particle entrainment over time*

To link the coherent structures with the TKE, quadrant analysis was used. The quadrant analysis was performed based on two different input vector fields in the investigation volume.

(1) The quadrant distribution in the investigation volume was conducted based on the Reynolds decomposed velocities (velocity fluctuations) u', v' and w' of the original vector fields for each test case 1S to 8S.

(2) The velocity vector field of the investigation volume was approximated (Eq. 3) based on the first five POD modes for each test case, and quadrant analysis was conducted. The results of the approximation were velocity vector fields containing approximately 50% of the TKE. Therefore, the POD method can also be seen as a lowpass filter because it selects flow structures containing a certain minimum amount of TKE for further investigations.

The different quadrant distributions, either based on the original Reynolds decomposed velocity vector fields (REY) or based on the approximated POD vector fields including the first five modes, are listed in Table 4 for each test case at the time of sediment particle entrainment. Here, the quadrant distributions define how much each single quadrant covers from the investigation volume.

The quadrant distributions of the Reynolds decomposed test cases show that at the time of sediment particle entrainment, mainly QI and QIV events are dominant. For all tests, except for test 6S, QIV motions are present at the time of sediment particle entrainment, covering at least 48.8% (test 1S) of the whole investigation volume. Outward interactions QI, at a minimum of 20.4% (test 8S) and a maximum of 43.9% (test 1S), were observed at sediment particle entrainment. Except for test 6S, these two quadrants cover a minimum of 90.3% (test case 3S) and a maximum of 99.9% (test case 7S) of the investigation volume at the time of sediment particle entrainment. In contrast to

Table 3   TKE per temporal mode a_k in percent based on the cumulative energy of the first five modes at the time of sediment particle entrainment (te)

	1S	2S	3S	4S	5S	6S	7S	8S
$a_{1,te}$	90.52	94.23	87.89	96.20	79.03	0.37	79.83	91.34
$a_{2,te}$	0.61	0.93	10.66	0.17	18.06	27.03	1.66	3.56
$a_{3,te}$	1.60	0.08	0.03	0.45	0.28	3.96	16.72	1.96
$a_{4,te}$	7.20	4.00	1.32	3.18	0.10	65.78	1.65	2.35
$a_{5,te}$	0.07	0.75	0.10	0.00	2.52	2.86	0.13	0.79

Table 4   Quadrant distribution in percent of the investigation volume for (i) Reynolds decomposed velocity vector fields (REY) and (ii) POD approximated velocity vector fields based on the first five modes for each test case at the time of sediment particle entrainment

	1S		2S		3S		4S		5S		6S		7S		8S	
	REY	POD	REY	POD	REY	POD	REY	POD	REY	POD	REY	POD	REY	POD	REY	POD
QI	43.9	13.8	31.0	13.4	27.4	6.9	22.2	1.9	29.7	10.6	16.0	17.4	22.0	28.2	20.4	1.7
QII	4.9	0.0	0.3	0.0	6.7	0.0	1.4	0.0	4.0	0.9	27.6	58.9	0.1	0.1	0.7	0.2
QIII	2.5	0.9	0.3	0.0	3.0	0.0	2.9	0.0	1.0	0.0	31.6	6.2	0.0	0.0	0.3	0.2
QIV	48.8	85.2	68.4	86.6	62.9	93.1	73.5	98.1	65.3	88.5	24.8	17.6	77.9	71.7	78.6	97.9

the other tests, where mainly QIV and QI occurred during sediment particle entrainment, these quadrants covered only 24.8% (QIV) and 16.0% (QI) for test 6S. During sediment particle entrainment, quadrants QII and QIII play a minor role, except for test 6S, where quadrant QII covers 27.6% and QIII covers 31.6% of the investigation volume. For the other test cases, the percentage of the mentioned quadrants is below 10%.

Considering the quadrant analysis of the approximated vector fields based on the first five most energetic modes, covering approximately 50% of the energy, it is visible that the most dominant quadrant of the Reynolds decomposition becomes even more pronounced in the approximated POD velocity field. For most test cases, QIV increases. Consequently, the increase in the proportion regarding the QIV quadrant leads to a reduction

of the other quadrants. The outward interactions of quadrant QI covered at least 20.4%, which dropped after the approximation to 1.7% (test 8S). In a similar manner, quadrants QII and QIII also played a minor role, except for test 6S. Here, the proportion of quadrant QII increased to 58.9% compared to Reynolds decomposed quadrant QII, where 27.6% was obtained. However, quadrant QIII was reduced from 31.6% (REY 6S) to 6.2% (POD 6S).

To link the observed quadrant events with the TKE emanating from of the first five modes, the quadrant distribution was calculated over the whole measurement time in the investigation volume. This makes it possible to evaluate which coherent structures, described as quadrants, are responsible for high or low TKE events. Figure 7 shows the TKE progression based
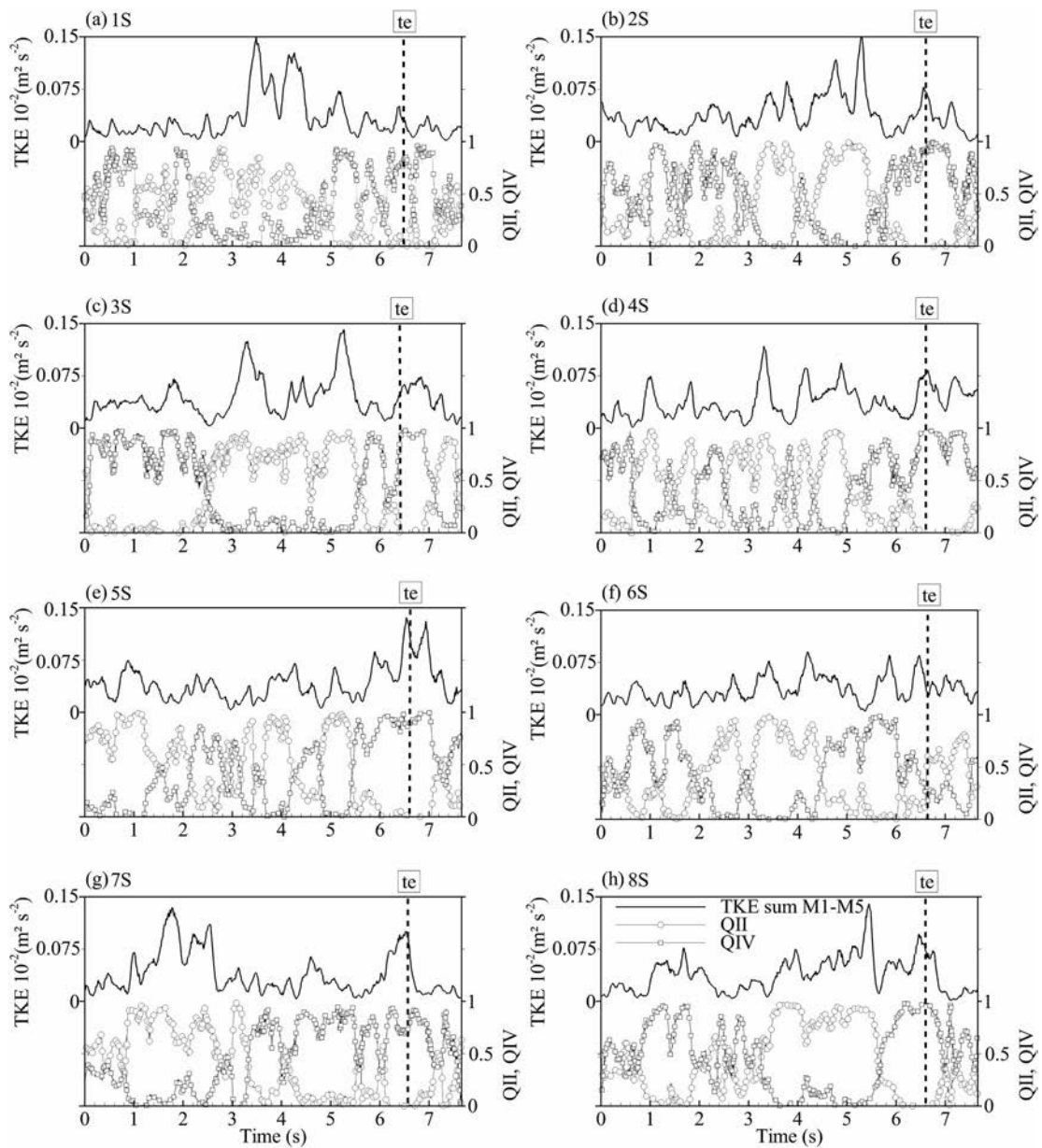

Figure 7   Quadrants QII and QIV plotted as light grey spheres (indicating ejections) and dark grey squares (indicating sweeps); the TKE (m² s⁻²) based on the first five modes is plotted as black solid line in the investigation volume over the measurement period. Time of entrainment is marked with a vertical dashed line and labelled with te. The right vertical axis related to quadrants, describes the proportion of ejections QII and sweeps QIV in the investigation volume. (a) 1S, (b) 2S, (c) 3S, (d) 4S, (e) 5S, (f) 6S, (g) 7S and (h) 8S

on the first five modes in comparison to the occurring fractions of the quadrant events QII and QIV. There, the quadrant events are related to the approximated vector fields based on the first five modes. Since QIV and QII were dominant at the time of sediment particle entrainment, only these events are shown in Fig. 7.

During the "highest" peaks concerning the TKE either a large fraction of QII (light grey line) or a large fraction of QIV (dark grey line) was present for all test cases. These motions (QII and QIV) alternated over time. Although the maximum TKE of the ejections exceeded the maximum TKE of sweeps for all test cases (except for test 5S), particle entrainment was never observed during the highest TKE events related to ejections. For tests 1S, 2S, 4S, 5S, 7S and 8S, sediment particle entrainment occurred at the highest TKE value during a sweep. Figure 7 shows for the abovementioned tests that sweep motions with a similar proportion, such as at the time of sediment particle entrainment but with less TKE in the investigation volume, did not lead to sediment particle entrainment. In the case of test 3S, the highest TKE peak of a sweep event was observed after approximately 1.8 s, but entrainment was not observed at that time. In contrast to the other tests, sediment particle entrainment in the case of 6S cannot be described with a TKE peak caused by QIV. This may be due to vortical motions in the flow field during sediment particle entrainment, where the quadrant analysis would result in a more even distribution, and hence dominant quadrant events such as sweeps would not be observed.

4.4 *Dominant spatial modes at sediment particle entrainment*

In summarizing the results, two different modes were dominant at sediment particle entrainment. As shown in Table 3, for all tests except for test 6S, most of the TKE is covered by the first temporal mode, with values of at least 79% during sediment particle entrainment. In contrast, for test 6S, most of the TKE (65.78%) was covered from the fourth mode at sediment particle entrainment. Here, one of the advantages of the POD method becomes obvious. While the temporal mode provides information about the TKE content, the spatial modes classify

the signatures of flow structures (Zhong et al., 2012). Hence, it is possible to visualize the dominant flow structures during sediment particle entrainment based on the TKE content. To analyse the different spatial signatures of the abovementioned dominant temporal modes, Fig. 8 illustrates the fourth spatial mode of test 6S and the first spatial mode of test 8S. Here, test 8S was chosen for comparison because the TKE content of the first mode corresponds approximately to the average under consideration for all conducted tests. However, the first spatial mode for all tests looks similar. The visualized spatial modes in Fig. 8 are slices through the investigation volume in a streamwise-vertical plane and in the middle axis of the flume and sediment particle. The sediment particle is outside of the vector field (investigation volume) at the horizontal position $X/h = 0$. In principle, the coefficient values of the temporal modes define the direction of the vectors in the spatial modes. Considering the first spatial mode (Fig. 8b), with positive coefficient values at sediment particle entrainment, a sweep motion with dimensions larger than the extracted slice was observed. Usually, the first mode is related to the largest coherent structures in the flow field (Zhong et al., 2015). The spatial signature of the fourth spatial mode for test 6S is shown in Fig. 4a. At the time of sediment particle entrainment, the coefficient value of the fourth mode is negative, which results in a counter-clockwise rotating (retrograde) vortex, which is marked with an ellipsoid (Fig. 8a). Between the flume bed and the observed retrograde vortex core, sweep motions are present. The observed retrograde vortex is located at the Y/h value of approximately 0.15, which is close to the outer edge of the logarithmic layer. Furthermore, a shear layer with an angle of approximately 20° was observed, which is shown as a line in Fig. 8a.

4.5 *Three-dimensional flow structures at sediment particle entrainment based on the approximated vector fields*

The approximated vector fields of the first five modes, covering approximately 50% of the TKE, were further three-dimensionally investigated in the whole investigation volume. For all tests except for test 6S, the first mode contributes the
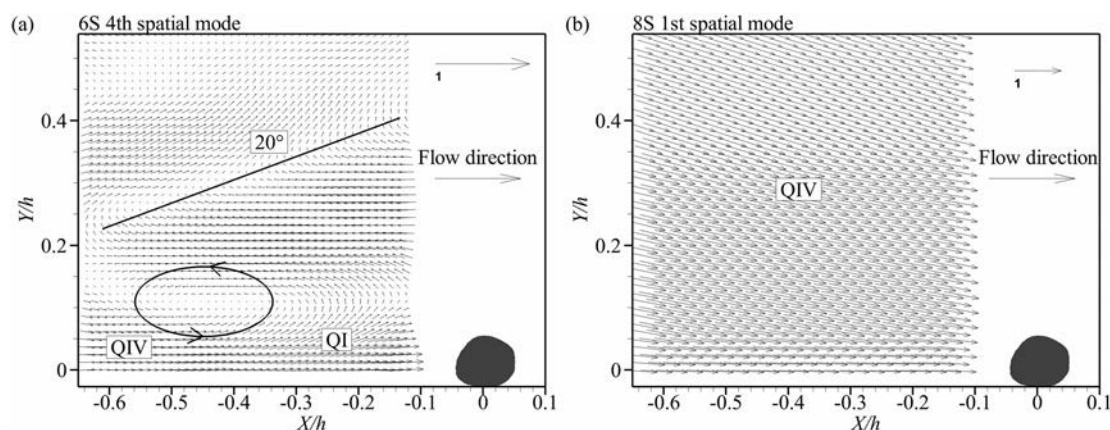

Figure 8　Comparison of the most TKE modes for test 6S and 8S. In case of 6S (a) the fourth spatial mode is shown and for test 8S (b) the first spatial mode. Flow direction is from left to right. Note that the reference vector in (a) is double the size of (b)
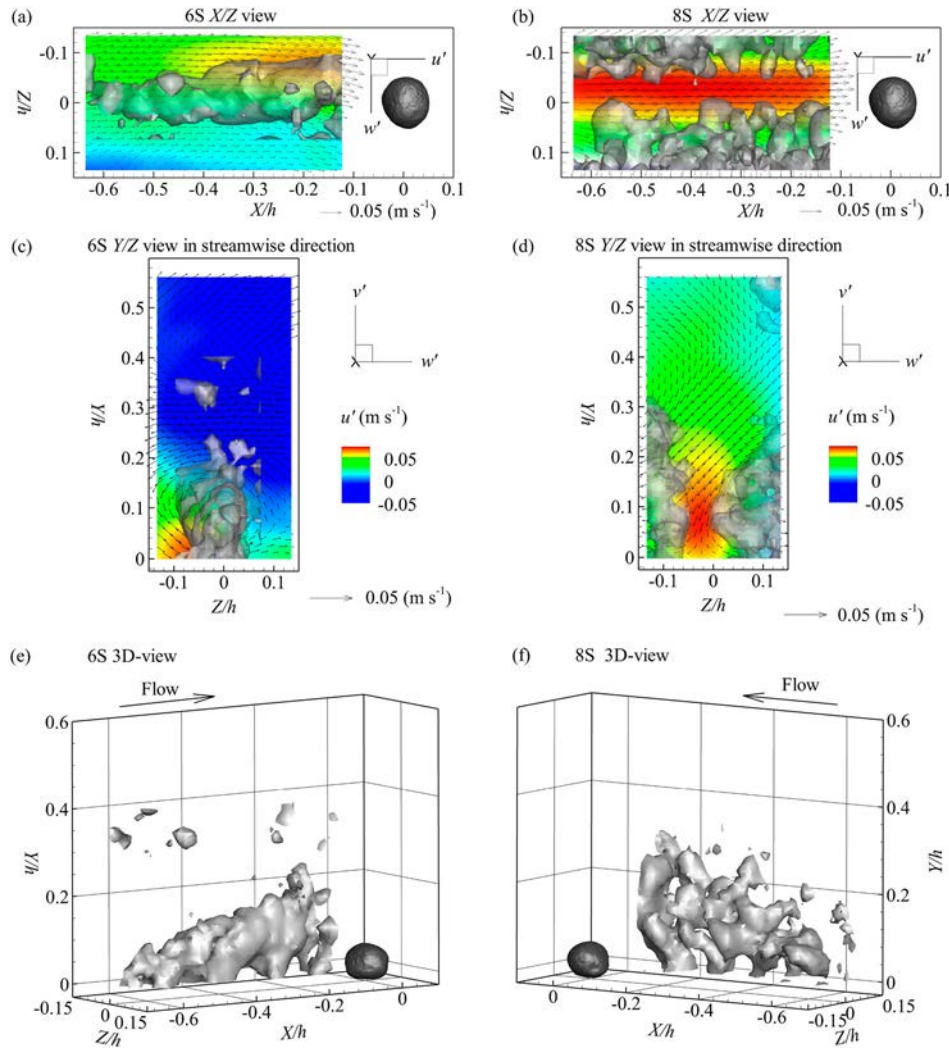
Figure 9   Comparison of the coherent structures based on the approximated vector fields between test 6S and 8S. Grey iso-surfaces correspond to the $Qc = 1$ (s^{-2}) and the vectors correspond to the approximated fluctuating velocities. Horizontal plane at a height of half the particle diameter (a) and (b), vertical plane view in streamwise direction one particle diameter upstream of the sediment particle (c) and (d) and 3D view with the flow direction from left to right (e) and from right to left (f) are shown. (f) shows just one of the two observed structures for a better visibility. Contours in (a), (b), (c) and (d) show the turbulent streamwise velocity u' in m s^{-1}. Note, that in (a), (b), (c) and (d) just every second vector is shown and a reference vector is given

most to the TKE at sediment particle entrainment; only tests 6S and 8S are shown for comparison in Fig. 9. In Fig. 9, coherent structures are visualized with grey iso-surfaces based on the Qc in X/Z, Y/Z and the 3D view. The Qc is defined as $1/2(||\boldsymbol{\Omega}||^2 - ||\mathsf{S}_r||^2)$, where $\boldsymbol{\Omega}$ is the mean vorticity vector and S_r is the mean rate-of-strain tensor. The used value of the Qc is the same for both test cases, i.e. $Qc = 1$. The vectors in the X/Z and Y/Z views correspond to the fluctuating velocities after the approximation. For test 6S, a streamwise elongated structure rotating in the Y/Z plan is visible at sediment particle entrainment. In contrast, test 8S shows two counter-rotating structures in the Y/Z plan, which are also elongated in the streamwise direction but are approximately double the vertical extension of the observed structure in test 6S. Between the counter-rotating vortices, the fluid was directed towards the flume bed (Fig. 9d), resulting in a sweep motion which was further visualized with

the contour corresponding to the streamwise velocity fluctuations u'. The direction of rotation is shown with black vectors in the Y/Z views of Fig. 9c and d. Both observed structures are larger than the length of the investigation volume, which is approximately 0.5 times the water depth (Fig. 9). Furthermore, a kind of developing or growing effect in the vertical direction Y, seen in the flow direction, is visible in the 3D views of Fig. 9e and f. Figure 9f shows only one of the streamwise elongated structures for better visibility.

5   Discussion

Researchers (Elyasi & Ghaemi, 2019; Liu et al., 2001; Roussinova et al., 2010; Wu & Christensen, 2010; Zhong et al., 2015) have reported that the first 10 POD modes contain

approximately 50–60% of the TKE. These studies used the POD method to investigate large- and very large-scale coherent structures. The present research showed that 50% of the TKE was covered by the first five to 12 POD modes (Fig. 4a). This is in line with the aforementioned references. In the conducted tests, a steep drop regarding the relative energies (Fig. 4b) is visible. While the first modes had an energy proportion of approximately 23–39%, the fifth mode, for example, showed relative energies of less than 3.5%. This is in accordance with the observed values of Roussinova et al. (2010) and Wu and Christensen (2010). Furthermore, the results based on the relative and cumulative energies for the tests with sediment particle entrainment in this paper showed that the first mode contained more TKE than the RF when considering the whole measurement period of the tests (Fig. 4). This leads to the assumption that large coherent motions are present during the tests with sediment particle entrainment, as the first mode corresponds to the largest structures in the flow field (Bomminayuni et al., 2011; Holmes et al., 1996).

When considering the first temporal modes of the tests, sediment particle entrainment was observed mostly during a peak of the normalized coefficient value and the consequent TKE. The first temporal mode covered at least 79% considering the cumulative TKE of the first five modes (Table 3). This was the case for all tests except for test 6S. Here, the fourth temporal mode contained the most TKE, which will be discussed later. The quadrant analysis was conducted based on the approximated vector fields with the first five spatial modes to link the energy peaks with outward interactions QI, ejections QII, inward interactions QIII and sweeps QIV. For all tests, except for test 6S, sweeps with a proportion of at least 71.7% in the investigation volume were present at the time of particle entrainment (Table 4). Ejections and sweeps were alternating during the measurement period and correlated well with the peaks of the TKE (Fig. 7). During the highest TKE events, ejections were present (except test 5S), but they played no role regarding sediment particle entrainment, while the highest TKE peaks related to a sweep, initiated sediment particle motion. Zhong et al. (2015) used the snapshot POD method for the investigation of LSM and VLSM based on 2D-PIV measurements in a smooth channel flow and found that peaks of the first temporal POD mode show dominant sweeps or ejections in the corresponding fluctuating velocity fields. If there was a positive peak, the fluctuating flow field was dominated by sweep events. Ejections were mainly observed at negative peaks of the temporal mode (Zhong et al., 2015). Similar observations have been made in our investigations. The results in this paper and from Zhong et al. (2015) show that peaks in the temporal modes, which are also peaks concerning the TKE in the flow field, contribute to positive Reynolds stress events (sweeps and ejections). This is in line with the observations of Liu et al. (2001), where based on low-order eigenmodes containing 50% of the TKE, the flow field contained approximately 2/3 to 3/4 of the total Reynolds shear stress.

The first and (except for test 6S, which is an exception) the fourth spatial modes contributed the most to the TKE during sediment particle entrainment; however, they showed two different signatures (Fig. 9). While sweep events were detected by the first spatial mode for all cases during sediment particle entrainment, the fourth mode consisted of a spanwise vortex (for tests 3S, 6S, 7S and 8S). In the case of test 6S, the fourth mode covered the most TKE at sediment particle entrainment. At that time, the flow field in the investigation volume consisted of a counter-clockwise rotating vortex (retrograde vortex). Natrajan et al. (2007) observed that retrograde vortices are common at the edge of the logarithmic layer $Y/h = 0.2$ and are often paired with prograde vortices (clockwise rotating vortices), which can be interpreted as signatures of so-called hairpin vortices. In the case of test 6S, the observed retrograde vortex at sediment particle entrainment is at $Y/h = 0.15$. A shear layer with an angle of approximately 20° was observed above the retrograde vortex. This angle is close to the observed angles of Adrian et al. (2000) during a passing hairpin vortex in the flow field. Beneath the retrograde vortex sweeps and outward interactions were present in test 6S at sediment particle entrainment. Shih et al. (2017) and Wu and Shih (2012) postulated that these quadrant events are responsible for single particle entrainment and are caused by a retrograde vortex in the flow field. Schobesberger et al. (2020) observed similar signatures in the flow field during sediment particle entrainment and showed that quadrant events akin to Wu and Shih (2012) were present during passing hairpin vortices at particle entrainment. Although the TKE in test 6S was lower than the other tests, sediment particle entrainment occurred. The reason for this could be the observed retrograde vortex (Fig. 8a) and the vortex tube (Fig. 9a, c and e), which possibly had a similar effect on sediment particle entrainment as the TKE peaks caused by sweeps. Therefore, it can be hypothesized that sediment particle entrainment was initiated by the observed vortex tube.

Based on Fig. 7, fluctuating sweeps and ejections covering the whole investigation volume during the measurement period were present. Similar alternating large-scale sweep and ejection events were found by Nakagawa and Nezu (1981), Shvidchenko and Pender (2001) and Zhong et al. (2015). These researchers hypothesized that alternating large-scale sweeps and ejections are signatures of VLSMs with sizes in the streamwise direction greater than 2–3 times the water depth, forming large counter-rotating streamwise tubes (with rotation in the Y/Z direction). VLSMs oscillate in the spanwise direction and are responsible for large sweep and ejection events related to a plane or in the streamwise/vertical slice (measured with free surface PTV and 2D-PIV from Tamburrino & Gulliver, 2007; Zhong et al., 2015). Similar observations were made by Cameron et al. (2017), who showed that streamwise velocity fluctuations are correlated with repeating counter-rotating vortices or patterns that are related to VLSMs. Furthermore, Cameron et al. (2019) conducted experiments to investigate the influence of VLSMs on the drag force

of immobile spherical particles with different protrusions used as roughness elements in open channel flows. Therefore, pre-multiplied spectral analyses were used, resulting in a bimodal shape of the drag force fluctuations, where a low-frequency and a high-frequency spectral peak were observed. As the low-frequency peak was related to high coherence between the drag force and the streamwise velocity components, Cameron et al. (2019) postulated/suggested that this was because of VLSMs. Based on the results of Cameron et al. (2019), VLSMs should be considered regarding sediment particle entrainment. The methods used by Cameron et al. (2017) and Cameron et al. (2019), such as spectral analysis and two-point correlation, provide important statistical information about the existence and influence of VLSMs on immobile particles. However, these methods are not suitable to investigate the instantaneous behaviour of VLSMs during sediment particle entrainment. To detect these three-dimensional vortical motions, appropriate measurement systems that are able to resolve three-dimensional velocity fields in a volume are necessary. The TOMO-PTV system and the POD method used for the present investigations were able to collect the needed three-dimensional data. Information about the shape and behaviour of the observed structures in a three-dimensional context during sediment particle entrainment could be gathered. Zhong et al. (2015) noted that the first POD mode is related to VLSMs, which he termed super-streamwise vortices. Signatures of VLSMs, such as those from Tamburrino and Gulliver (2007), Zhong et al. (2015) and Cameron et al. (2017), were found at sediment particle entrainment in all cases (except for 6S) in the present study. Two counter-rotating vortical structures elongated in the streamwise direction were present (Fig. 9) during sediment particle entrainment. The fluid in between the two counter-rotating vortices was transferred towards the flume bed causing a sweep motion. In Fig. 9f, the counter rotating streamwise vortex pairs have a vertical extent of approximately $Y/h = 0.2$. This is consistent with the findings of Balakumar and Adrian (2007) where the wavelengths of VLSMs exist approximately to the edge of the logarithmic region. However, based on the restricted investigation volume a visualization was just partly possible. The observed structure in Fig. 9f was stable over a time period of approximately 0.7 s, which can also be seen in Fig. 7h, where the sweep motion was present in the investigation volume. This can be seen as a result of the counter rotating vortices observed in this paper and e.g. from Zhong et al. (2015). Estimating the streamwise extent of the approximately 0.7 s long stable structure with the mean streamwise velocity U would lead to a length of approximately three times the water depth. Based on the partly visualized signatures and the estimated length ($\sim 3h$), the observed structures in Fig. 9f might be part of a VLSM. At sediment particle entrainment, the TKE peak was caused by a sweep event. It is well accepted that sweep motions correspond to higher drag forces (Schmeeckle et al., 2007) and impulses (Dwivedi et al., 2011), which underlines their importance.

6 Conclusion

Under the given experimental design, the following conclusions can be drawn.

- During the tests with sediment particle entrainment the first temporal modes contained more relative TKE than the reference case.
- At sediment particle entrainment, the first temporal modes showed positive peak values except for test 6S. Compared to the TKE contained in the first five modes, the first mode dominated from at least 79% up to 96% of the TKE proportion. For test 6S, the fourth mode was dominant at sediment particle entrainment, showing a retrograde vortex in the spatial mode.
- It was found that during high TKE events, ejection and sweep events were mainly evident in the flow field, covering up to 100% of the investigation volume. These opposite quadrant events alternated over time. Ejections were responsible for the highest TKE peaks during the measurement period, but they did not lead to particle entrainment. Although the maximum TKE peaks evoked by sweeps are smaller than the ejection TKE peaks, sweeps were responsible for sediment particle entrainment.
- Streamwise elongated counter rotating vortices were found based on the approximated vector fields during sediment particle entrainment. Based on their direction of rotation fluid was transferred towards the bed and a sweep emerged. Based on the observed signatures a VLSM during sediment particle entrainment can be suggested.
- For test 6S, sediment particle entrainment was caused by a retrograde vortex or vortex tube containing less TKE in the lower modes compared to the other test cases. This leads to the hypothesis that these vortical motions have a similar influence on sediment particle entrainment.

Notation

A	=	streamwise length of sediment particle (m)
B	=	vertical length of sediment particle (m)
$\boldsymbol{b}$	=	coefficient vector (m s^{-1})
C	=	spanwise length of sediment particle (m)
d	=	particle diameter (here the average of A, B and C was used) (m)
F	=	Froude number (–)
g	=	gravity (m s^{-2})
h	=	water depth (m)
$\bar{h}$	=	mean water depth (m)
M	=	number of snapshots (–)
N	=	number of spatial points (–)
P	=	depth of pocket (m)
Q	=	discharge (l s^{-1})
Qc	=	Q-criterion (s^{-2})
R	=	hydraulic radius (m)
R$_e$	=	Reynolds number (–)
R$_{e*}$	=	particle Reynolds number (–)
S	=	slope (%)
S$_r$	=	mean rate-of-strain tensor (s^{-1})
U	=	mean flow velocity (m s^{-1})
u	=	instantaneous streamwise velocity (m s^{-1})
u'	=	streamwise velocity fluctuations (m s^{-1})
u^*	=	shear velocity (m s^{-1})
V	=	mean vertical velocity (m s^{-1})
v	=	instantaneous vertical velocity (m s^{-1})
v'	=	vertical velocity fluctuations (m s^{-1})
W	=	mean spanwise velocity (m s^{-1})
w	=	instantaneous spanwise velocity (m s^{-1})
w'	=	spanwise velocity fluctuations (m s^{-1})
X	=	horizontal or streamwise coordinate (m)
Y	=	vertical coordinate (m)
Z	=	spanwise coordinate (m)
$\boldsymbol{a_k}$	=	temporal modes (m s^{-1})
θ	=	Shields parameter (–)
θ_c	=	critical Shields parameter (–)
λ_k	=	eigenvalues (m^2 s^{-2})
v	=	kinematic viscosity (m^2 s^{-1})
ρ	=	water density (kg m^{-3})
ρ_s	=	sediment particle density (kg m^{-3})
σ_i	=	turbulence intensities of velocity components (m s^{-1})
τ	=	shear stress (N m^{-2})
$\boldsymbol{\phi_k}$	=	spatial modes (–)
$\boldsymbol{\Omega}$	=	mean vorticity vector (s^{-1})

ORCID

JOHANNES SCHOBESBERGER http://orcid.org/0000-0002-6052-5752

DOMINIK WORF http://orcid.org/0000-0002-6289-4420
SENCER YÜCESAN http://orcid.org/0000-0002-4223-0889
CHRISTOPH HAUER http://orcid.org/0000-0001-8704-2198
HELMUT HABERSACK http://orcid.org/0000-0002-1598-6138
CHRISTINE SINDELAR http://orcid.org/0000-0002-2132-3138

References

Adrian, R. J. (2007). Hairpin vortex organization in wall turbulence. *Physics of Fluids*, *19*(4), 1–16. https://doi.org/10.1063/1.2717527

Adrian, R. J., & Marusic, I. (2012). Coherent structures in flow over hydraulic engineering surfaces. *Journal of Hydraulic Research*, *50*(5), 451–464. https://doi.org/10.1080/00221686.2012.729540

Adrian, R. J., Meinhart, C. D., & Tomkins, C. D. (2000). Vortex organization in the outer region of the turbulent boundary layer. *Journal of Fluid Mechanics*, *422*, 1–54. https://doi.org/10.1017/S0022112000001580

Bagherimiyab, F., & Lemmin, U. (2018). Large-scale coherent flow structures in rough-bed open-channel flow observed in fluctuations of three-dimensional velocity, skin friction and bed pressure. *Journal of Hydraulic Research*, *56*(6), 806–824. https://doi.org/10.1080/00221686.2017.1416686

Balakumar, B.J. & Adrian, R.J. (2007). Large- and very-large-scale motions in channel and boundary-layer flows. *Philosophical Transactions of the Royal Society A: Mathematical, Physical and Engineering Sciences*, *365*(1852), 665–681. https://doi.org/10.1098/rsta.2006.1940

Berkooz, G., Holmes, P., & Lumley, J. L. (1993). The proper orthogonal decomposition in the analysis of turbulent flows. *Annual Review of Fluid Mechanics*, *25*(1). 539–575. https://doi.org/10.1146/annurev.fl.25.010193.002543

Bomminayuni, S., Stoesser, T., & Asce, M. (2011). Turbulence statistics in an open-channel flow over a rough bed. *Journal of Hydraulic Engineering*, *137*(11), 1347–1358. https://doi.org/10.1061/(ASCE)HY.1943-7900.0000454

Cameron, S. M., Nikora, V. I., & Marusic, I. (2019). Drag forces on a bed particle in open-channel flow: Effects of pressure spatial fluctuations and very-large-scale motions. *Journal of Fluid Mechanics*, *863*, 494–512. https://doi.org/10.1017/jfm.2018.1003

Cameron, S. M., Nikora, V. I., & Stewart, M. T. (2017). Very-large-scale motions in rough-bed open-channel flow. *Journal of Fluid Mechanics*, *814*, 416–429. https://doi.org/10.1017/jfm.2017.24

Celik, A. O., Diplas, P., & Dancey, C. L. (2013). Instantaneous turbulent forces and impulse on a rough bed: Implications for initiation of bed material movement. *Water Resources Research*, *49*(4), 2213–2227. https://doi.org/10.1002/wrcr.20210

Deng, S., Pan, C., Wang, J., & He, G. (2018). On the spatial organization of hairpin packets in a turbulent boundary layer at low-to-moderate Reynolds number. *Journal of Fluid Mechanics*, *844*, 635–668. https://doi.org/10.1017/jfm.2018.160

Diplas, P., & Dancey, C. L. (2013). Coherent flow structures, initiation of motion, sediment transport and morphological feedbacks in rivers. In J.G. Venditti, J.L. Best, M. Church and R.J. Hardy (Eds.), *Coherent flow structures at earth's surface* (pp. 289–307). John Wiley & Sons, Ltd. https://doi.org/10.1002/9781118527221.ch19

Diplas, P., Dancey, C. L., Celik, A. O., Valyrakis, M., Greer, K., & Akar, T. (2008). The role of impulse on the initiation of particle movement under turbulent flow conditions. *Science*, *322*(5902), 717–720. https://doi.org/10.1126/science.1158954

Dwivedi, A., Melville, B., & Shamseldin, A. Y. (2010). Hydrodynamic forces generated on a spherical sediment particle during entrainment. *Journal of Hydraulic Engineering*, *136*(10), 756–769. https://doi.org/10.1061/(ASCE)HY.1943-7900.0000247

Dwivedi, A., Melville, B. W., Shamseldin, A. Y., & Guha, T. K. (2011). Flow structures and hydrodynamic force during sediment entrainment. *Water Resources Research*, *47*(1), 1–18. https://doi.org/10.1029/2010WR009089

Elyasi, M., & Ghaemi, S. (2019). Experimental investigation of coherent structures of a three-dimensional separated turbulent boundary layer. *Journal of Fluid Mechanics*, *859*, 1–32. https://doi.org/10.1017/jfm.2018.788

Holmes, P., Lumley, J. L., & Berkooz, G. (1996). *Turbulence, coherent structures, dynamical systems and symmetry*. Cambridge University Press.

Hurther, D., Lemmin, U., & Terray, E. A. (2007). Turbulent transport in the outer region of rough-wall open-channel flows: the contribution of large coherent shear stress structures (LC3S). *Journal of Fluid Mechanics*, *574*, 465–493. https://doi.org/10.1017/S0022112006004216

Kline, S. J., Reynolds, W. C., Schraub, F. A., & Runstadler, P. W. (1967). The structure of turbulent boundary layers. *Journal of Fluid Mechanics*, *30*(4), 741–773. https://doi.org/10.1017/S0022112067001740

Kostas, J., Soria, J., & Chong, M. S. (2005). A comparison between snapshot POD analysis of PIV velocity and vorticity data. *Experiments in Fluids*, *38*(2), 146–160. https://doi.org/10.1007/s00348-004-0873-4

Lichtneger, P., Sindelar, C., Schobesberger, J., Hauer, C., & Habersack, H. (2020). Experimental investigation on local shear stress and turbulence intensities over a rough non-uniform bed with and without sediment using 2D particle image velocimetry. *International Journal of Sediment Research*, *35*(2), 193–202. https://doi.org/10.1016/j.ijsrc.2019.11.001

Liu, Z., Adrian, R. J., & Hanratty, T. J. (2001). Large-scale modes of turbulent channel flow: transport and structure. *Journal of Fluid Mechanics*, *448*, 53–80. https://doi.org/10.1017/S0022112001005808

Lu, S. S., & Willmarth, W. W. (1973). Measurements of the structure of the Reynolds stress in a turbulent boundary layer. *Journal of Fluid Mechanics*, *60*(03), 481. https://doi.org/10.1017/S0022112073000315

Lumley, J. L. (1967). The structure of inhomogeneous turbulent flows. In A. M. Yaglam, & V. Tatarsky (Eds.), *Proceedings of the international colloquium on the fine-scale structure of the atmosphere and its influence on radio wave propagation* (pp. 166–178). Doklady Akademii Nauk SSSR.

Meyer-Peter, E., & Mueller, R. (1948). Formula for bed load transport. In *Proc., 2nd Int. association for hydro-environment engineering and research congress*, June 7–9, (pp. 39–64). Stockholm: International Association for Hydro-Environment Engineering and Research.

Nakagawa, H., & Nezu, I. (1981). Structure of space-time correlations of bursting phenomena in an open-channel flow. *Journal of Fluid Mechanics*, *104*, 1–43. doi:10.1017/S0022112081002796

Natrajan, V. K., Wu, Y., & Christensen, K. T. (2007). Spatial signatures of retrograde spanwise vortices in wall turbulence. *Journal of Fluid Mechanics*, *574*, 155–167. https://doi.org/10.1017/S0022112006003788

Nezu, I. (1977). *Turbulence structure in open channel flows* (Ph.D. Thesis). Kyoto Univ., Kyoto, Japan. http://resolver.tudelft.nl/uuid:a41f39c2-fce6-4647-bd7a-1d412c720ed7

Nezu, I., & Nakagawa, H. (1993). *Turbulence in open-channel flows*. Balkema.

Roussinova, V., Shinneeb, A.-M., & Balachandar, R. (2010). Investigation of fluid structures in a smooth open-channel flow using proper orthogonal decomposition. *Journal of Hydraulic Engineering*, *136*(3), 143–154. https://doi.org/10.1061/(asce)hy.1943-7900.0000155

Saha, P., Biswas, G., Mandal, A. C., & Sarkar, S. (2017). Investigation of coherent structures in a turbulent channel with built-in longitudinal vortex generators. *International Journal of Heat and Mass Transfer*, *104*, 178–198. https://doi.org/10.1016/j.ijheatmasstransfer.2016.07.105

Schanz, D., Schröder, A., Gesemann, S., Michaelis, D., & Wieneke, B. (2013). 'Shake the box': A highly efficient and accurate Tomographic Particle Tracking Velocimetry (TOMO-PTV) method using prediction of particle positions. *10th International Symposium on Particle Image Velocimetry – PIV13*. Delft, The Netherlands, July 1–3, 1–13.

Schmeeckle, M. W., Nelson, J. M., & Shreve, R. L. (2007). Forces on stationary particles in near-bed turbulent flows. *Journal of Geophysical Research: Earth Surface*, *112*(2), 1–21. https://doi.org/10.1029/2006JF000536

Schneiders, J. F. G., & Sciacchitano, A. (2017). Track benchmarking method for uncertainty quantification of particle tracking velocimetry interpolations. *Measurement Science and Technology*, *28*(6), 1–12. https://doi.org/10.1088/1361-6501/aa6a03

Schobesberger, J., Lichtneger, P., Hauer, C., Habersack, H., & Sindelar, C. (2020). Three-dimensional coherent flow structures during incipient particle motion. *Journal of Hydraulic Engineering*, *146*(5), 1–12. https://doi.org/10.1061/(ASCE)HY.1943-7900.0001717

Shields, A. (1936). *Anwendung der Aehnlichkeitsmechanik und der Turbulenzforschung auf die Geschiebebewegung*. Mitteilungen No.26 der Preußischen Versuchsanstalt für Wasserbau und Schiffbau, Berlin.

Shih, W. R., Diplas, P., Celik, A. O., & Dancey, C. (2017). Accounting for the role of turbulent flow on particle dislodgement via a coupled quadrant analysis of velocity and pressure sequences. *Advances in Water Resources*, *101*(Jan), 37–48. https://doi.org/10.1016/j.advwatres.2017.01.005

Shvidchenko, A. B., & Pender, G. (2001). Large flow structures in a turbulent open channel flow. *Journal of Hydraulic Research*, *39*(1), 109–111. https://doi.org/10.1080/00221680109499810

Sirovich, L. (1987). Turbulence and the dynamics of coherent structures. Part I: Coherent structures. Part II: Symmetries and transformations. Part III: Dynamics and scaling. *Quarterly of Applied Mathematics*, *45*(3), 561–571. https://doi.org/10.1090/qam/910462

Smart, G. M., & Jaeggi, M. N. R. (1983). *Sediment transport on steep slopes*. Zürich: Mitteilungen der Versuchsanstalt für Wasserbau, Hydrologie und Glaziologie, 64.

Tamburrino, A., & Gulliver, J. S. (2007). Free-surface visualization of streamwise vortices in a channel flow. *Water Resources Research*, *43*(11). https://doi.org/10.1029/2007WR005988

Valyrakis, M., Diplas, P., Dancey, C. L., Greer, K., & Celik, A. O. (2010). Role of instantaneous force magnitude and duration on particle entrainment. *Journal of Geophysical Research: Earth Surface*, *115*(C2), F02006. https://doi.org/10.1029/2008JF001247

Vowinckel, B., Jain, R., Kempe, T., & Fröhlich, J. (2016). Entrainment of single particles in a turbulent open-channel flow: A numerical study. *Journal of Hydraulic Research*, *54*(2), 158–171. https://doi.org/10.1080/00221686.2016.1140683

Wieneke, B. (2008). Volume self-calibration for 3D particle image velocimetry. *Experiments in Fluids*, *45*(4), 549–556. https://doi.org/10.1007/s00348-008-0521-5

Wu, F. C., & Shih, W. R. (2012). Entrainment of sediment particles by retrograde vortices: Test of hypothesis using near-particle observations. *Journal of Geophysical Research: Earth Surface*, *117*(3), 1–20. https://doi.org/10.1029/2011JF002242

Wu, Y., & Christensen, K. T. (2010). Spatial structure of a turbulent boundary layer with irregular surface roughness. *Journal of Fluid Mechanics*, *655*, 380–418. https://doi.org/10.1017/S0022112010000960

Yücesan, S., Schobesberger, J., Sindelar, C., Hauer, C., Habersack, H., & Tritthart, M. (2020). *Large eddy simulation of a sediment particle under entrainment conditions*. [Research paper submitted on December 16th, 2019 and under review in Journal of Hydraulic Research].

Zhong, Q., Li, D., Chen, Q., & Wang, X. (2015). Coherent structures and their interactions in smooth open channel flows. *Environmental Fluid Mechanics*, *15*(3), 653–672. https://doi.org/10.1007/s10652-014-9390-z

Zhong, Q., Li, D. X., Chen, Q. G., & Wang, X. K. (2012) Coherent structure models for open channel flows. *Journal of Tsinghua University*, *52*(6), 730–737 (Science and Technology).